Supplementary Documentation for "Inferring the Mean Effective Elastic Thickness of the Outer Ice Shell of Enceladus from Diurnal Crustal Deformation"

In S1, we describe the governing equations for our tidal loading boundary value problem and our solution method (1.1), benchmark our solutions against analytic and numerical tidal loading models (1.2), and verify that results on models with heterogeneities are not subject to inaccuracy due to our choice of mesh sizing parameters (1.3) or our choice of weak-zone elastic moduli (1.4).

S1

1.1 Tidal Loading Formulation

Following Aagaard et al. (2007), we formulate and solve a boundary value problem appropriate for tidal loading. We solve the weak form the quasi-static equation of motion in cartesian directions i for a body subject to stresses σ_{ij} and specific forces f_i over the volume W and a weighting function ϕ_i (the symbol , denotes derivative with respect to a direction):

$$\int_W (\sigma_{ij,j} + f_i)\ \phi_i\ dW = 0 \tag{1}$$

Following the Galerkin approach, we formulate our weighting function ϕ_i as an n-dimensional linear combination of linear basis (i.e., shape) functions N^n scaled by coefficients c_i^n and our trial solution (i.e., for displacement u_i) as an m-dimensional linear combination of linear basis functions N^m scaled by coefficients a_i^m :

$$\phi_i = \sum_n c_i^n N^n \tag{2a}$$

$$u_i = \sum_m a_i^m N^m \tag{2b}$$

Considering the divergence theorem for stresses in W, substituting our formulation for the weighting function, and recognizing that the equation of motion's weak form is equivalent to the strong form for arbitrary weighting function coefficients c_i^n allows us to rewrite Equation 1 as a sum of integrals over surfaces S subject to tractions T_i and over W subject to specific forces f_i:

$$-\int_W \sigma_{ij} N^n_{,j} dW \; + \int_S T_i N^n dS \; + \int_W f_i N^n dW = 0 \tag{3}$$

We expand each term in Equation 3 according to our tidal loading formulation. We rewrite the first term (from the left) as a combination of shape functions scaled by a rank-4 stiffness tensor C_{ijqw}. We select parameters in C_{ijqw} appropriate for a linear isotropic material with a shear modulus G and bulk modulus μ:

$$-\int_W \sigma_{ij} N^n_{,j} dW = \int_W \sum_m \frac{1}{4} C_{ijqw} (N^m_{,w} + N^m_{,q})(N^n_{,j} + N^n_{,i}) a^m_i dW \tag{4}$$

We subdivide the second term of Equation 3 to treat tractions at the outer surface S^0 (i.e., T^0_i) and the inner surface S^{int} (i.e., T^{int}_i) of our geometry. For small displacements induced by a loading potential V (See Equation 2 of the main text), we can write T^{int}_i and T^0_i as dependent upon radial displacements at the boundaries of our geometry $\sum_m a^m_i N^m (\mathbf{e}_i \cdot \mathbf{e}_s)$ (see Equation 2; $\mathbf{e}_i$ and $\mathbf{e}_s$ respectively denote unit vectors perpendicular to the surface of the geometry and the evaluated direction), the density of ice ρ_{ice} and ocean water ρ_w, gravitational acceleration at the inner and outer surfaces g_{int} and g_0 (see Table 2 in the main text), and self-gravitation induced by radial displacements throughout our geometry V^{sg}. Here, we treat self-gravitational potential V^{sg} as resulting from small perturbations to the driving potential V and therefore as a separate (i.e., uncoupled) term as per Taylor's approximation theorem:

$$\int_{S^0} T^0_i N^n dS = \int_{S^0} \sum_m a^m_i N^m (\mathbf{e}_i \cdot \mathbf{e}_s) \rho_{ice} g_0 (\mathbf{e}_s \cdot \mathbf{e}_i) N^n dS \tag{5a}$$

$$\int_{S^{int}} T^{int}_i N^n dS = \int_{S^{int}} (\sum_m a^m_i N^m (\mathbf{e}_i \cdot \mathbf{e}_s)(\rho_{ice} - \rho_w) g_{int} + \rho_w V + \rho_w V^{sg})(\mathbf{e}_s \cdot \mathbf{e}_i) N^n dS \tag{5b}$$

The specific force (i.e., third) term in Equation 3 is rewritten as the gradient of the driving and self-gravitational potentials scaled by ice density as per Newton's second law:

$$\int_W f_i N^n dW = \int_W (\rho_{ice} \nabla (V + V^{sg}) \cdot \mathbf{e}_i) N^n dW \tag{6}$$

Terms from Equations 6, 5a, and 5b constitute the 'body' F^b, 'ocean traction' F^o, and 'topographic' F^t forces discussed in Section 2.2 of the main text (see supplementary equation S5 of Souček et al. 2016):

$$F^b = \int_W (\rho_{ice} \nabla (V + V^{sg}) \cdot \mathbf{e}_i) N^n dW \tag{7a}$$

$$F^o = \int_{S^{int}} (\rho_w V + \rho_w V^{sg})(\mathbf{e}_s \cdot \mathbf{e}_i) N^n dS \tag{7b}$$

$$\begin{aligned} F^t = & \int_{S^0} \sum_m a_i^m N^m (\mathbf{e}_i \cdot \mathbf{e}_s) \rho_{ice} g_0 (\mathbf{e}_s \cdot \mathbf{e}_i) N^n dS \\ & + \int_{S^{int}} (\sum_m a_i^m N^m (\mathbf{e}_i \cdot \mathbf{e}_s)(\rho_{ice} - \rho_w) g_{int}) (\mathbf{e}_s \cdot \mathbf{e}_i) N^n dS \end{aligned} \tag{7c}$$

To compute V^{sg}, we combine solutions to the Poisson's equation (i.e., potentials) evaluated at nodes with radial locations r^n arising from displacements linearly mapped into spherical harmonics at inner V_0^{sg} and outer surfaces V_{int}^{sg} (i.e., via the rank-4 tensors H_{lknm}^0 and H_{lknm}^{int} evaluated at mean radial locations R_{int} and R_0 respectively with degree l and order k) and universal gravitational constant $\mathcal{G}$ (i.e., as discussed in Hemingway & Mittal (2019) cf. Equation 4). We assume V^{sg} arises purely from the movement of mass at the boundaries of our domain (i.e., the inner and outer surfaces of the crust) and so ignore effects due to the changes in density on V^{sg}:

$$V^{sg} = V_{int}^{sg} + V_0^{sg} \tag{8}$$

$$V_{int}^{sg} = \sum_l \sum_k \frac{4\pi \mathcal{G} r^n}{2l+1} (\rho_w - \rho_{ice}) \sum_m H_{lknm}^0 a_i^m N^m (\mathbf{e}_i \cdot \mathbf{e}_s) \big(\frac{R_0}{r^n}\big)^{l+2} \tag{9a}$$

$$V_0^{sg} = \sum_l \sum_k \frac{4\pi \mathcal{G} r^n}{2l+1} \rho_{ice} \sum_m H_{lknm}^{int} a_i^m N^m (\mathbf{e}_i \cdot \mathbf{e}_s) \big(\frac{r^n}{R_{int}}\big)^{l-1} \tag{9b}$$

We combine terms from Equations 4, 5a, 5b, 6, 8, and 9 to formulate a Jacobian A_{ij}^{nm} as a superposition of tensors integrated over our domain volume ${}_W A_{ij}^{nm}$, outer surface ${}_{S^0} A_{ij}^{nm}$, and inner surface ${}_{S^{int}} A_{ij}^{nm}$.

$$A_{ij}^{nm} = {}_W A_{ij}^{nm} + {}_{S^0} A_{ij}^{nm} + {}_{S^{int}} A_{ij}^{nm} \tag{10}$$

$$
{}_{W}A_{ij}^{nm} = \int_{V} (\frac{1}{4} C_{ijqw}(N_{,w}^{m} + N_{,q}^{m})(N_{,j}^{n} + N_{,i}^{n}) + (\rho_{ice}\nabla(\sum_{l}\sum_{k} \frac{4\pi\mathcal{G}r^{n}}{2l+1}((\rho_{w} - \rho_{ice}) H_{lknm}^{0}(\mathbf{e}_{i}\cdot\mathbf{e}_{s})\big(\frac{R_{0}}{r^{n}}\big)^{l+2} + \rho_{ice}H_{lknm}^{int}(\mathbf{e}_{i}\cdot\mathbf{e}_{s})\big(\frac{r^{n}}{R_{int}}\big)^{l-1})) \cdot \mathbf{e}_{i})N^{n}N^{m})dW \tag{11a}
$$

$$
{}_{S^{int}}A_{ij}^{nm} = \int_{S^{int}} ((\rho_{w}\sum_{l}\sum_{k} \frac{4\pi\mathcal{G}r^{n}}{2l+1}((\rho_{w} - \rho_{ice})H_{lknm}^{0}(\mathbf{e}_{i}\cdot\mathbf{e}_{s})\big(\frac{R_{0}}{r^{n}}\big)^{l+2} + \rho_{ice}H_{lknm}^{int} (\mathbf{e}_{i}\cdot\mathbf{e}_{s})\big(\frac{r^{n}}{R_{int}}\big)^{l-1}))(\mathbf{e}_{s}\cdot\mathbf{e}_{i}) + (\mathbf{e}_{i}\cdot\mathbf{e}_{s})(\rho_{ice} - \rho_{w})g_{int}(\mathbf{e}_{s}\cdot\mathbf{e}_{i}))N^{n}N^{m}dS \tag{11b}
$$

$$
{}_{S^{0}}A_{ij}^{nm} = \int_{S^{0}} (\mathbf{e}_{i}\cdot\mathbf{e}_{s})\rho_{ice}g_{0}(\mathbf{e}_{s}\cdot\mathbf{e}_{i})N^{n}N^{m}dS \tag{11c}
$$

We can also combine terms from Equations 5a, 5b, and 6 to write a force vector b_i^n:

$$
b_{i}^{n} = -\int_{W} (\rho_{ice}\nabla V\cdot\mathbf{e}_{i})N^{n}dW - \int_{S^{int}} \rho_{w}V(\mathbf{e}_{s}\cdot\mathbf{e}_{i})N^{n}dS \tag{12}
$$

Finally, we assemble Equations 10, 11, and 12 to form a linear system and solve for displacement coefficients a_i^m.

$$
A_{ij}^{nm}a_{i}^{m} = b_{i}^{n} \tag{13}
$$

1.2 Benchmarking

We benchmark our tidal loading formulation on *Base* models against analytic solutions using the spectral solver software package SATStress, a widely used tool within the planetary science community to predict diurnal (and fluid) Love number values and stress fields on planetary bodies (Wahr et al., 2009). SATStress solves the equation of motion for tidally-loaded multi-layered spherically symmetric bodies accounting for self-gravitation and viscous effects. Figure 1 shows predictions of Love number values from SATStress across our range of modelled $\tilde{d}_{el}$ values. Within SATStress, we specify a multi-layered body with an outer ice layer and underlying ocean consistent with the rheological parameters in Table 2 (see main text), an ice viscosity ν = 1e16 Pa-s (Friedson & Stevenson, 1983), an ocean shear modulus G_o = 1e-20 GPa, and an ocean viscosity ν_o = 1e-20 Pa-s. Love number values between numerical and analytical models agree to within <0.1% across all $\tilde{d}_{el}$ values. Possible additional minor differences between predictions

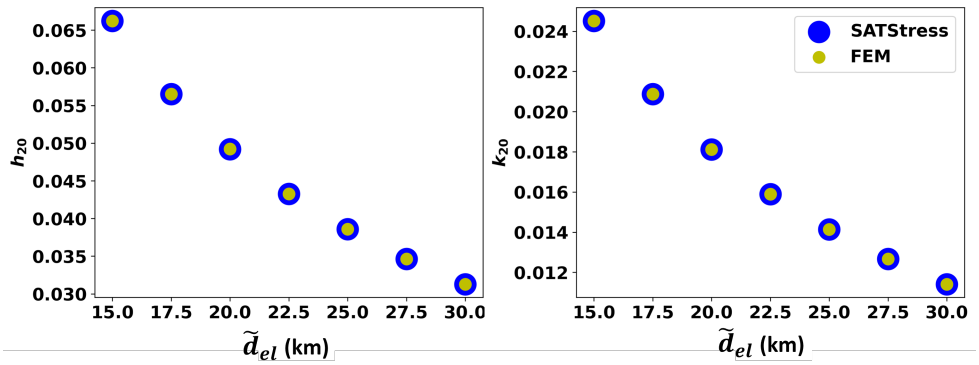

Figure 1. Comparison of analytic and FEM Love number results for several values of $\tilde{d}_{el}$ on spherically symmetric (*Base*) models. Love numbers plotted against $\tilde{d}_{el}$ for analytic models using SATStress (blue dots) and using the FEM formulated here (yellow dots).

from either set of results may result from our lack of accounting for changes in ice shell rheology due to volumetric expansion/contraction or viscous effects within the ice shell during tidal loading (See Wahr et al. (2006), for details).

We additionally compare model results from this work with results from Souček et al. (2016). Figure 2 shows displacement magnitude fields at three different time indices in the tidal cycle (t=0.0 T (periapse) , 0.2 T, and 0.4 T, where T is the orbital period T = 33 hrs) for models in Souček et al. (2016) (top row) and this work (bottom). We deactivate self-gravitation on *Base* models assign weak zones (with assigned bulk modulus $\mu_{WZ} = 10^{-5}\mu$ and shear modulus $G_{WZ} = 10^{-5}G$) to regions surrounding the Tiger Stripes for model comparisons. We find we are able to largely reproduce results from Souček et al., (2016) both quantitatively (i.e., peak displacement magnitude values correspond to within <10%) and qualitatively. Slight differences in displacement field characteristics persist surrounding the weak zone regions due to methodological differences in the implementation of adaptive mesh sizing, the assignment of reduced elastic moduli (i.e., the location of the Tiger Stripes and the shear modulus reduction away from fault planes), or the use of different shape functions (i.e., linear vs. quadratic) between models.

1.3 Mesh Convergence Test

We perform a mesh convergence test to confirm that Love number results from models with structural heterogeneities are not sensitive to chosen mesh sizing parameters. Figure 3 shows Love number values evaluated from models with only weak zones at chasma,

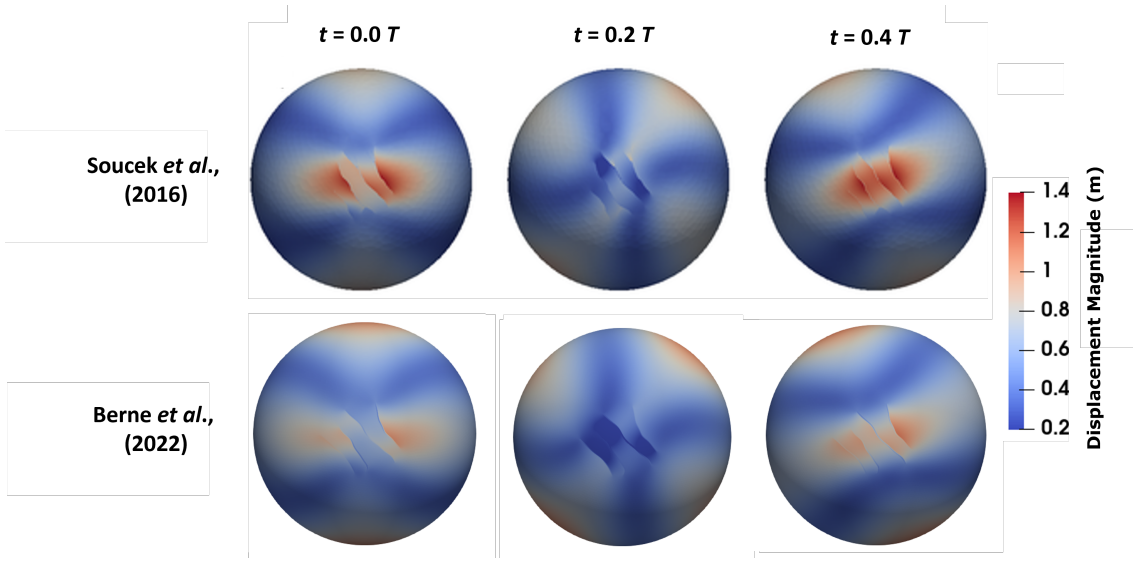

Figure 2. Qualitative comparison of our FEM results with results from Souček et al. (2016) (top row) and this work (bottom row) for models with weak zones at Tiger Stripe locations viewed facing the South Pole. Fields denote the magnitude of the displacement vector evaluated at the outer surface of deformed geometries. The top row and colorbar of this Figure adapted from top row of Figure 3 of Souček et al. (2016). We assign weak zone bulk moduli μ_{WZ}/μ=10^{-5} and shear moduli G_{WZ}/G=10^{-5} for our simulations in accordance with the formulation of weak zones described in Souček et al. (2016).

Tiger Stripe, and circum-tectonic boundary locations (i.e., *WZ* models) and $\tilde{d}_{el} = 15$ km meshed with specified minimum cell side lengths S_{min}= 6, 5, 4, 3, 2, and 1 km. We additionally show example snapshots of the radial displacement fields between our *WZ* model relative to our *Base* model for geometries with $\tilde{d}_{el} = 15$ km across our range of tested S_{min} values. Results from Figure 3 demonstrate that both Love number results and overall radial displacement fields are insensitive to chosen minimum cell size for values of $S_{min} <$ 3 km. We accordingly assign $S_{min} = 1$ km for all models discussed in this work.

1.4 Choice of Weak Zone Elastic Parameters

We evaluate results from models with weak zones at chasma, Tiger Stripe, and circum-tectonic boundary locations (i.e., *WZ* models) to confirm that Love number outputs are not sensitive to our choice of weak zone shear modulus. Figure 4 shows Love number values evaluated from *WZ* models with $\tilde{d}_{el} = 15$ km and specified weak zone moduli across $10^{-8} < G_{WZ}/G < 10^{0}$. We additionally show example snapshots of radial displacement fields from our *WZ* models relative to our *Base* model with $\tilde{d}_{el} = 15$ km across our range of tested G_{WZ} values. Results from Figure 4 demonstrate that both Love number results and overall radial displacement fields are insensitive weak zone shear modulus for $G_{WZ}/G < 10^{-4}$. These results are consistent with those described in the supplementary documentation of Souček et al. (2016) but extend to inferences of displacement away from the Tiger Stripes and for instances of non-zero bulk modulus within weak zones.

References

Aagaard, B., Williams, C., & Knepley, M. (2007). PyLith: A Finite-Element Code for Modeling Quasi-Static and Dynamic Crustal Deformation. *Eos*, *88(52)*.

Friedson, A. J., & Stevenson, D. J. (1983). Viscosity of rock-ice mixtures and applications to the evolution of icy satellites. *Icarus*, *56*. doi: 10.1016/0019-1035(83)90124-0

Hemingway, D. J., & Mittal, T. (2019). Enceladus's ice shell structure as a window on internal heat production. *Icarus*, *332*. doi: 10.1016/j.icarus.2019.03.011

Souček, O., Hron, J., Běhounková, M., & Čadek, O. (2016). Effect of the tiger stripes on the deformation of Saturn's moon Enceladus. *Geophysical Research*

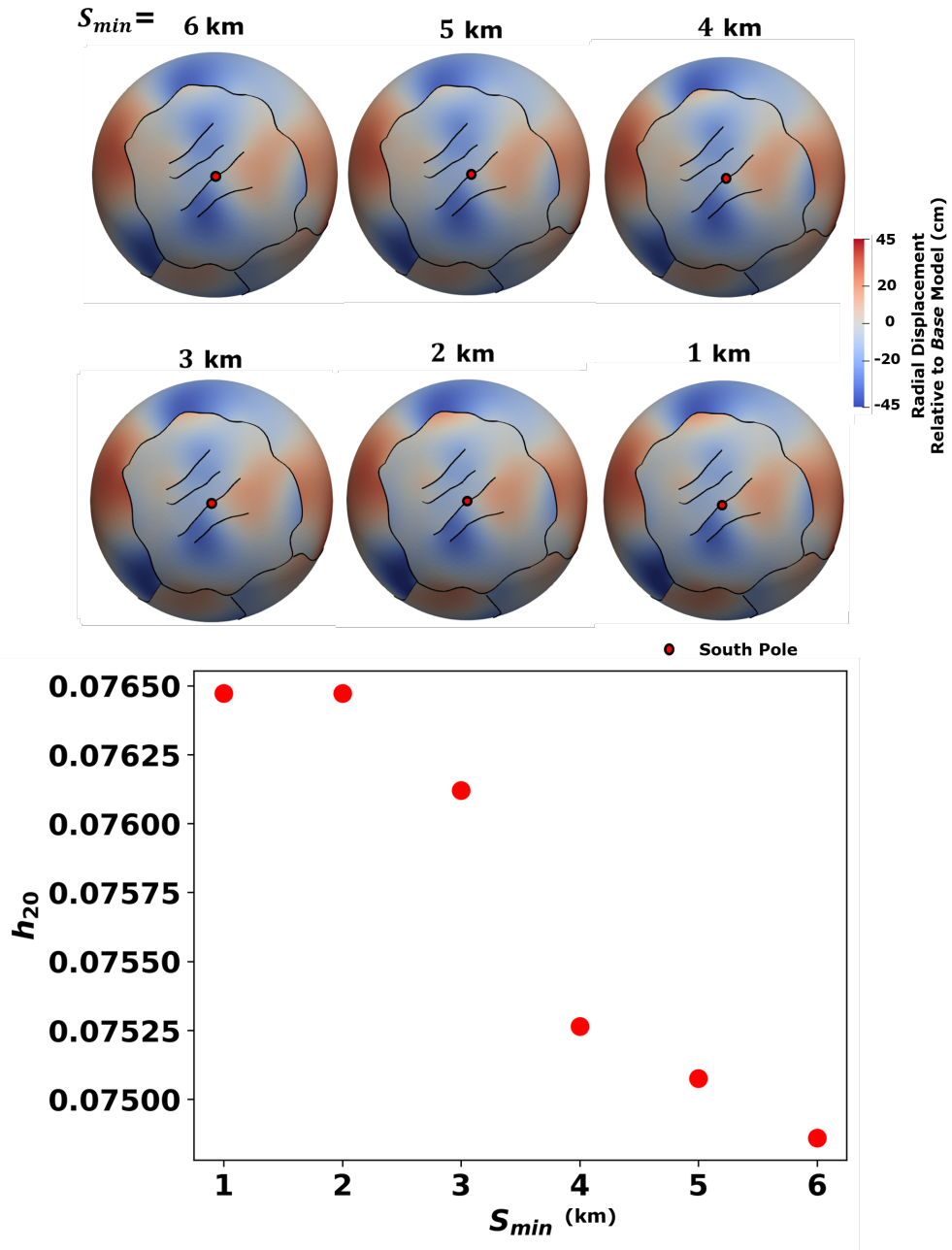

Figure 3. Results evaluated at periapse for *WZ* models ($\tilde{d}_{el}$ = 15 km) for a range of S_{min}. We show radial displacement fields viewed facing upwards towards the South Pole (top) and h^d_{20} Love number results we use to track the sensitivity of results due to changes in S_{min} (bottom)

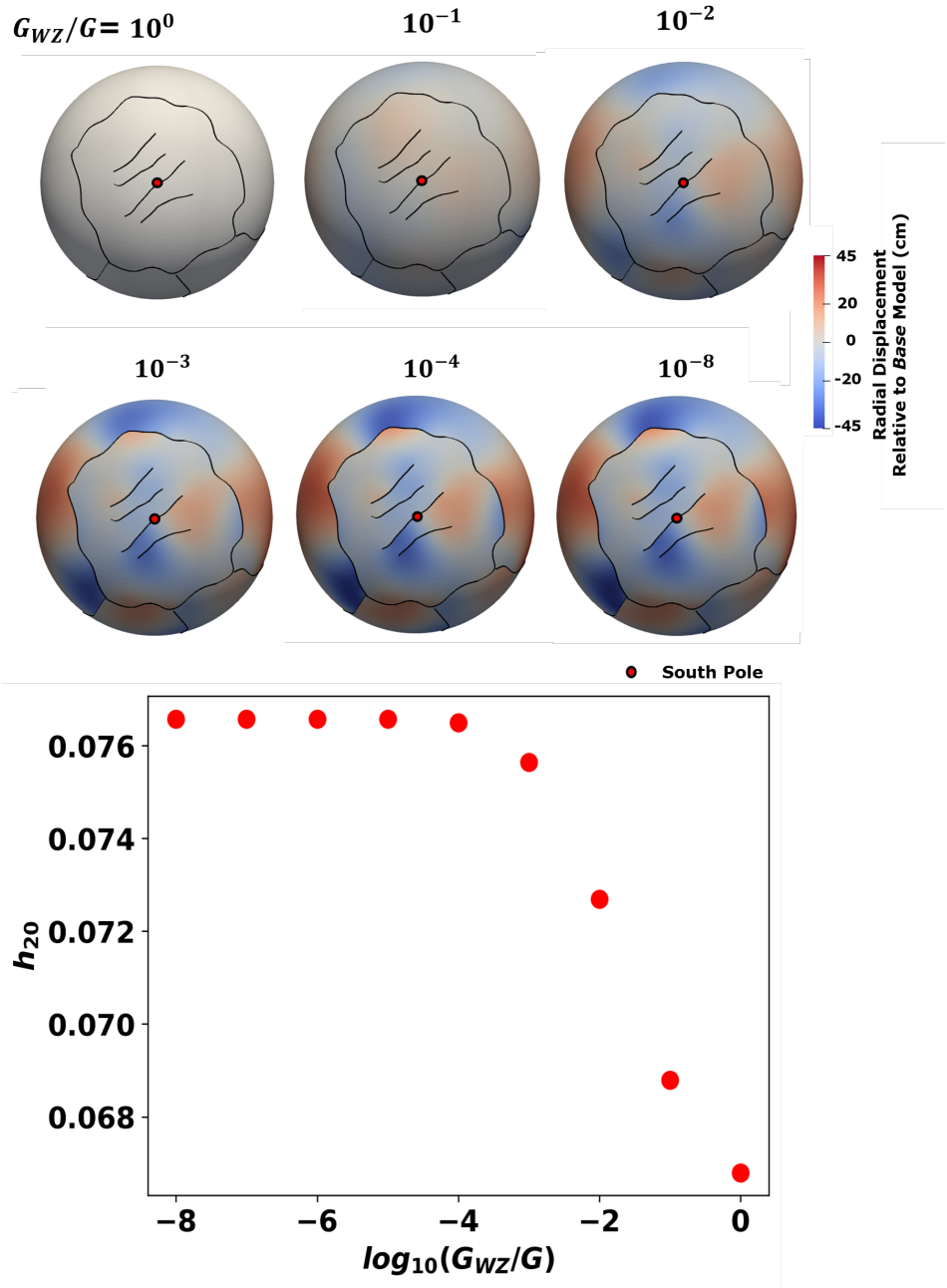

Figure 4. Results evaluated at periapse for WZ models ($\tilde{d}_{el} = 15$ km) across several values of G_{WZ}. We show radial displacement fields viewed facing upwards towards the SP (top) and h^d_{20} Love number results we use as a proxy for effective model stiffness.

Letters, *43*(14). doi: 10.1002/2016GL069415

Wahr, Selvans, Z. A., Mullen, M. E., Barr, A. C., Collins, G. C., Selvans, M. M., & Pappalardo, R. T. (2009). Modeling stresses on satellites due to nonsynchronous rotation and orbital eccentricity using gravitational potential theory. *Icarus*, *200*(1). doi: 10.1016/j.icarus.2008.11.002

Wahr, Zuber, M. T., Smith, D. E., & Lunine, J. I. (2006). Tides on Europa, and the thickness of Europa's icy shell. *Journal of Geophysical Research E: Planets*, *111*(12). doi: 10.1029/2006JE002729